A continuum voxel approach to model flow in 3D fault networks: a new way to obtain up-scaled hydraulic conductivity tensors of grid cells

André Fourno, Christophe Grenier, Abdelhakim Benabderrahmane, Frédérick Delay

A continuum voxel approach to model flow in 3D fault networks: a new way to obtain up-scaled hydraulic conductivity tensors of grid cells

André Fourno[1], Christophe Grenier[2], Abdelhakim Benabderrahmane[3], Frederick Delay[4].

[1] Corresponding author, IFP Energies Nouvelles, 1&4 Avenue du Bois Préau 92500 Rueil-Malmaison, France. Tel.:+33 1 47 52 72 57. Fax:+33 1 47 52 60 31. andre.fourno@ifpenergiesnouvelles.fr

[2] Laboratoire des Sciences du Climat et de l'Environnement UMR 8212 CNRS-CEA-UVSQ, CEA/Orme des Merisiers 91191 Gif-sur-Yvette Cedex, France.

[3] ANDRA, DRD/EAP, Parc de la Croix Blanche, 1-7 rue Jean Monnet, 92298 Châtenay-Malabry, France.

[4] LHyGeS - UMR CNRS 7517. 1, Rue Blessig 67084 Strasbourg cedex, France.

Abstract

Modelling transfers in fractured media remains a challenging task due to the complexity of the system geometry, high contrasts and large uncertainties on flow and transport properties. In the literature, fractures are classically modelled by equivalent properties or are explicitly represented. The new Fracture Continuum Voxel Approach (FCVA), is a continuum approach partly able to represent fracture as discrete objects; the geometry of each fracture is represented on a regular meshing associated with a heterogeneous field of equivalent flow properties. The mesh-identification approach is presented for a regular grid. The derivation of equivalent voxel parameters is developed for flow simulated with a Mixed Hybrid Finite Element (MHFE) scheme. The FCVA is finally validated and qualified against some reference cases. The resulting method investigates multi-scaled fracture networks: a small scale homogenized by classical methods and large discrete objects as that handled in the present work.

Highlights

- An accurate mapping of discrete fracture networks onto a regular mesh is obtained

- A full hydraulic conductivity tensor in each mesh is needed to model fracture fluxes
- hydraulic properties preserve continuity of fluxes between neighbouring meshes
- Various hydraulic behaviour at fracture intersections can be modelled

Keywords

Fractured media, Up-scaling, Equivalent hydraulic conductivity tensors, Mixed hybrid finite elements.

1 Introduction

Within the research community involved in the studies of transfers in fractured media, special emphasis is regularly put on experimentation and simulation of flow and transport in fractured media for various reasons, e.g., prediction of oil production (Bourbiaux, 2010), improvement of storage capacity for gas (Iding and Ringrose 2009; Ringrose et al., 2011), safety assessment of nuclear waste repositories (Geotrap, 20002; Chapman and McCombie, 2003) etc. Several constraints make this modelling work a challenging task: the geometrical complexity of the system, the scarcity of available data, and the strong contrasts in parameter values between mobile and immobile zones (Bear et al., 1993; Neuman, 2005).

Transfers in fractured media have already been subjected to intense modelling work (e.g., Bear et al., 1993; Koudina et al., 1998; Berkowitz, 2002; Bogdanov et al., 2003; Karimi-Fard et al., 2004; Adler et al., 2005). A large diversity of models exists, with differences on both the fracture medium conceptualization and the way to represent physically and numerically the flow and transport mechanisms. These differences make comparisons of the approaches a complex task (Selroos et al., 2001). For spatially distributed models relying on Eulerian approaches to flow and transport, the meshed representation of the fracture medium is the first difficulty to overcome. The fracture network geometry can be explicitly accounted for or replaced by equivalent properties mapped onto a regular or irregular (geological) grid mesh. It is then referred to the so-called discrete and continuous approaches, respectively.
For discrete approaches, fractures are often modelled by means of planar objects (e.g., Cacas et al., 1990; Dershowitz et al., 1991; Cvetkovic et al., 2004; Adler et al., 2005; Pichot et al., 2010;

de Dreuzy et al., 2012; Noetinger and Jarrige, 2012; for Discrete Fracture Network approaches) or linear objects with the consequence of limiting flow to channels within fracture planes and at fracture intersections (channel models or pipe network models, Dverstorp et al., 1992; Moreno and Neretnieks, 1993; Tsang and Neretnieks, 1998; Ubertosi et al., 2007). Nevertheless, specific meshing efforts are required which become cumbersome when a large number of fractures has to be represented, for instance with small scale fractures. Some attempts however based on corner-point grids and finite-volume approaches mixing two-dimensional and one-dimensional elements for fracture planes and fracture intersections, respectively are able to partly homogenize complex fracture fields (Karimi-Fard et al., 2006).

On the other hand, the so-called continuous approaches are commonly used in petroleum engineering and hydrology for simulating reservoirs especially when the latter are of sedimentary type. As suggested by their name, the classical single continuum approaches consider a single equation to cope with flow in both fractures and matrix. However, fractured rocks are often depicted by two (or more) media with contrasted properties, for example, to separate the fracture network from the matrix medium. The subsequent dual-continuum approaches (Barrenblatt et al. 1960; Warren and Root, 1963; Delay et al., 2007) deal with one equation of flow in each medium and an additional term of transfer between the two media for closing the problem (see the extended review of existing approaches in Berkowitz, 2002). According to the degree of complexity introduced in the system, the resolution of flow can either be performed numerically in both media, or the incidence of matrix on flow in fractures is handled by means of analytical solutions (Grenier and Benet, 2002). Continuous approaches rely upon the definition of a Representative Elementary Volume (REV), defined for instance as the minimal block size for which the mean hydraulic conductivity value stabilizes when increasing the size of the block (Long et al., 1982). At the REV scale, it becomes possible to calculate equivalent hydraulic properties that take into account the presence of fractures. Unfortunately, the REV does not always exist, as with the cases of poorly connected fracture networks (e.g., fracture network at the percolation threshold) or networks of large faults with characteristic lengths of the same order as the size of the investigated domain. The equivalent properties (e.g., hydraulic permeability for flow resolution) may be obtained analytically (Oda, 1985, 1986; Lee et al., 1995; Pan et al., 2010) or numerically (Bourbiaux et al., 1998; Koudina et al., 1998; Delorme et al., 2008) and allow an accurate modelling of the flow in the fracture medium even if the fracture network geometry is simplified.

The line of research conducive to the Fracture Continuum Voxel Approach (FCVA) is a kind of combination between continuous and discrete approaches. Basically, it is grounded in the mapping of a fracture network onto a regular grid for solving flow and transport with classical numerical approaches. One might consider that mapping fractures results into unrealistic representations of the medium and the topic could be debated for a long time. It is obvious that mapping fractures onto regular grids belongs to homogenization techniques that discard pinpoint accuracy and focus on the macroscopic behaviour of a system. The first advantage is the relative ease with which the model can be manipulated in complex problems such as inversion of field data. But as a matter of trade-off, one may also lose some elementary mechanisms while ignoring whether or not they have some importance at large scale. On the other hand, some exhaustive representations of fracture networks do not lose the elementary mechanisms but are cumbersome in terms of computation costs. This feature makes them hard to invert and unsuited to operational tasks as for instance evaluating uncertainty. Usually, the complete fracture field of an underground reservoir is unknown and, even with fine representations of fracture fields; the latter can be unrealistic, or at least very uncertain. Evaluating uncertainty can rely upon Monte-Carlo simulations duplicating numerous networks but usually, accurate representations of fracture networks do not lend themselves to this exercise because the meshing procedure is time consuming.

When mapping fractures onto regular grids, it is obvious that the network representation is less accurate. But duplicating networks for evaluating uncertainty does not result in cumbersome calculations. Iterative inversion procedures can be launched with reasonable computation costs. Incidentally within this inversion framework, one may raise that field (experimental) data are often uncertain and inaccurate in terms of spatial and temporal resolutions. These resolutions are sufficient for the rough mapping of fractures whereas they do not yield good conditioning of models based on the exhaustive representation of fractured media. In the end, our aim is to provide a versatile tool able to treat various types of fracture networks whilst avoiding intense meshing effort, and able to integrate explicit fractures as well as a single or dual porosity background.

The fracture medium is investigated first to identify the main features that will be explicitly represented (main fluid conductors at the scale of the studied block) whereas minor fractures, i.e., fractures whose lengths are smaller than the size of the mesh elements, are homogenized and associated with the matrix zones. Though a small fracture can be highly conductive, it will yield a very permeable matrix mesh which is handled as a porous continuum. When mapping (homogenizing) fractures onto a regular grid, one focuses actually on the capability of the fractures to connect very distant points. A dense network of short fractures will in comparison behave as a local patch of high conductivity. Even though the numerical model used below can handle matrix with various properties, the matrix is here overlooked for the sake of simplicity. The non-homogenised fractures are mapped onto a regular grid by applying direct equivalent properties to meshes cross-cut by the fracture network and the final outcome is a heterogeneous hydraulic conductivity field. Several published methods handle such systems with a regular grid where heterogeneous specific hydrodynamic properties justify the difference between fractures and matrix blocks. For instance, the fields of properties can be obtained from realizations of stochastic processes derived from sites data (Tsang et al., 1996; Gomez-Hernandez et al., 2000) or from analytical calculations based on geometrical considerations between the fractures and the regular mesh (Tanaka et al., 1996; Svensson 2001a, 2001b; Langevin, 2003; Reeves et al., 2008; Hirano et al., 2010). A major drawback associated with these approaches is that fractures are represented in a smeared way, meaning that fracture apertures are in practice spread over several juxtaposed grid cells, thus yielding numerical prints of fractures much wider than they should be. In addition, the equivalent properties implemented are expressed as scalar values instead of tensors (e.g., Oda, 1985, 1986), leading to imprecisions in the simulated fluxes within fracture objects.

The present work develops a new way to obtain the hydraulic properties of a fracture network mapped onto a regular mesh. The originality of this approach is grounded in a direct control of fluxes and the use of equivalent hydraulic conductivity tensors. To underline the importance of this point, a special focus will be put on the fact that a full tensor is needed to upscale fracture properties. Nevertheless, for computational time optimisation, the proposed equivalent hydraulic conductivity tensors are diagonal, which will appear in the sequel as a good assumption for sub-vertical or sub-horizontal fault networks.

Thanks to the use of tensors and an improved fracture representation, the mesh smearing is limited and the precision of results increases. The numerical scheme considered (a Mixed Hybrid Finite Element (MHFE) scheme) is well known for ensuring flux conservation between edges (or facets) of neighbouring elements (Younes et al., 2010). Equivalent properties are calculated for this specific MHFE scheme whilst preserving its properties of flux conservation. As shown later, the precision in the results is mainly related to the considered mesh size and can be easily controlled. This feature allows us to perform either a "reference" calculation by using a very refined grid or duplicate similar calculations on coarser grids. Simulations can serve as well to simplify the fracture network by removing fractures weakly impacting the system (as was proposed by Grenier et al., 2009).

The FCVA is here presented for the reductionist case of flow limited to fractures in a three-dimensional network. The fractures discussed in the sequel are planar objects but could also be warped ones. Provided that warped fractures can be approximated by pieces of planar objects juxtaposed by common vertices, the mapping procedure is similar to that presented for planar fractures. The numerical code was implemented and tested in Cast3M (2009), a simulation platform developed in mixed hybrid finite elements by the CEA (Commissariat à l'Energie Atomique). In the sequel, the grid element identification procedure for a single 3D fracture is described in Section 2. The equivalent permeability tensor is derived in Section 3. Finally, the approach is validated and qualified against some basic cases in Section 4.

2 Voxel fracture meshing and associated flow connectivity

The basic meshing of the fractured medium is a three-dimensional regular grid. The mapping of fractures onto the grid makes the fractures to look like stairs. Figure 1 depicts a fracture network mapped onto a regular cubic gridding (see as well Langevin, 2003; Hirano et al., 2010). The aim is to represent each fracture with a minimum of cells given that two neighbouring cells should have a common facet. For instance, the aperture of each fracture should be limited to one cell and fracture intersections limited to one irregular row of connecting cells. This requires an algorithm where the contacts between each step of the stairs representing a fracture must be designed taking into account that two adjacent steps should keep contact by only two lines of cells.

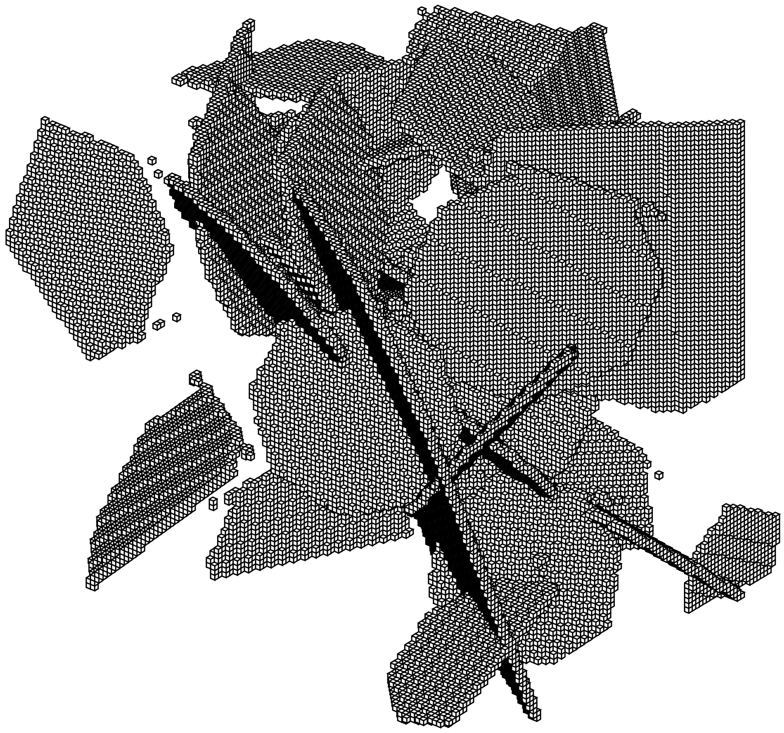

Fig. 1. An example of voxel grid for a network of planar fractures

The geometrical procedure to identify the fracture cells can be summarized as follows:

- Calculate the distance between the corners of cells of the regular grid and the fracture plane.
- Mark the grid elements that have corners at both a positive and a negative distance from the fracture plane as elements crossed by the fracture plane.
- Suppress elements as indicated below to obtain the correct connectivity of the adjacent steps.

We note that the three points evoked above also apply to pieces of planar objects approximating the shape of a warped fracture. The key point of suppressing some cells is illustrated in Figure 2.

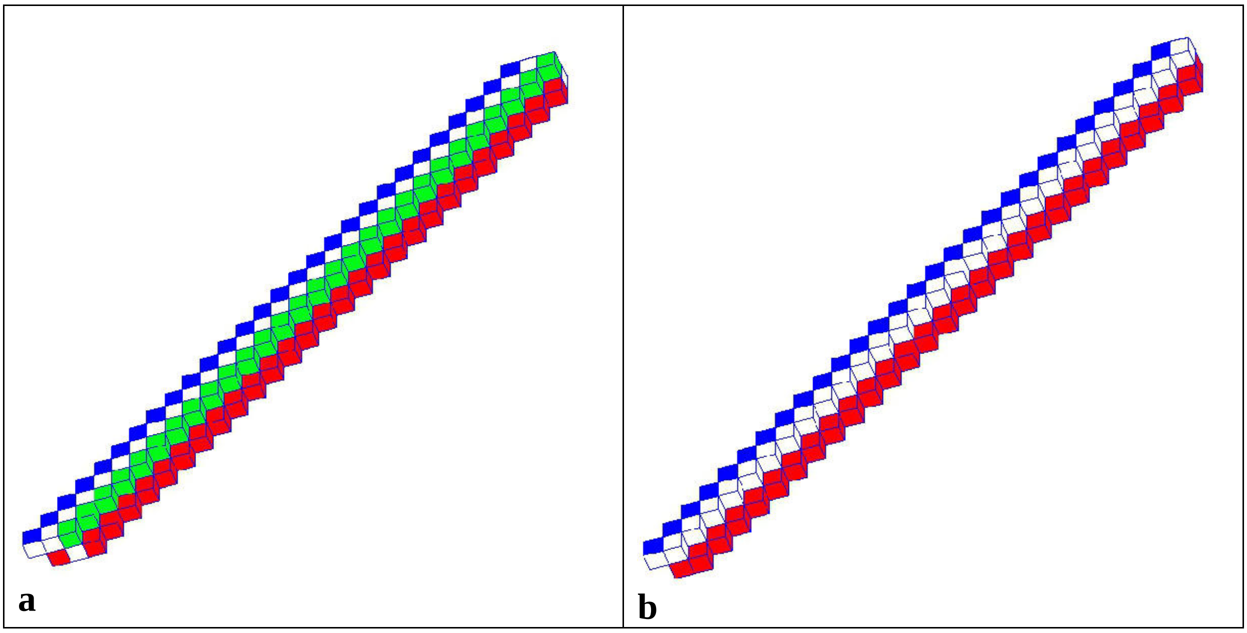

Fig. 2. Examples of step-shaped sets of meshes discretizing a fracture. a: steps that do not respect the optimal contact between stairs; b: steps with optimal contact (only two rows of cells in contact) between stairs.

The portion of fracture in Figure 2a is comprised of two steps and the connection between these steps is assured by four lines of cubic elements. The green cubes of the top step are located at the top of cubes which are not the border cubes of the bottom step. These green cubes of the top step have to be suppressed while the white ones of the bottom step are preserved. Finally, the correct fracture representation is given in Figure 2b and, by duplicating this elimination procedure over all steps, the fracture is represented with the minimum number of elements connected by their facets. The procedure is applied for each fracture of the network and the fracture intersections are simply obtained as the resulting intersections of the fracture geometries.

In addition, within each fracture meshing, groups of cells have to be identified in view of the equivalent approach presented below: the cells constituting the fractures are separated in two distinct subsets. The first set, noted S set for "simple set", is that enclosing cells whose neighbouring cells are all in the same plane. The second set, noted C (C stands for complex), regroups two lines of N cells (denoted A and B in Figure 3). The property of a C set is to connect two groups of S sets (i.e., C is the vertical part of a stair connecting two horizontal steps). For both sets S and C, there are no fluxes through the top and bottom facets of cells. Two angles, θ and β, are used to define the fracture plane orientation. θ (respectively, β) is the angle between the horizontal plane *x-y* and the fracture intersection (trace) on the vertical plane *x-z* (respectively, *y-z*). It must be noted that the configuration presented in Figure 3 occurs for $45° \ge \beta > \theta \ge 0°$. In the sequel, this configuration will be studied as the example of reference and the procedure dealing with other orientations will be then derived.

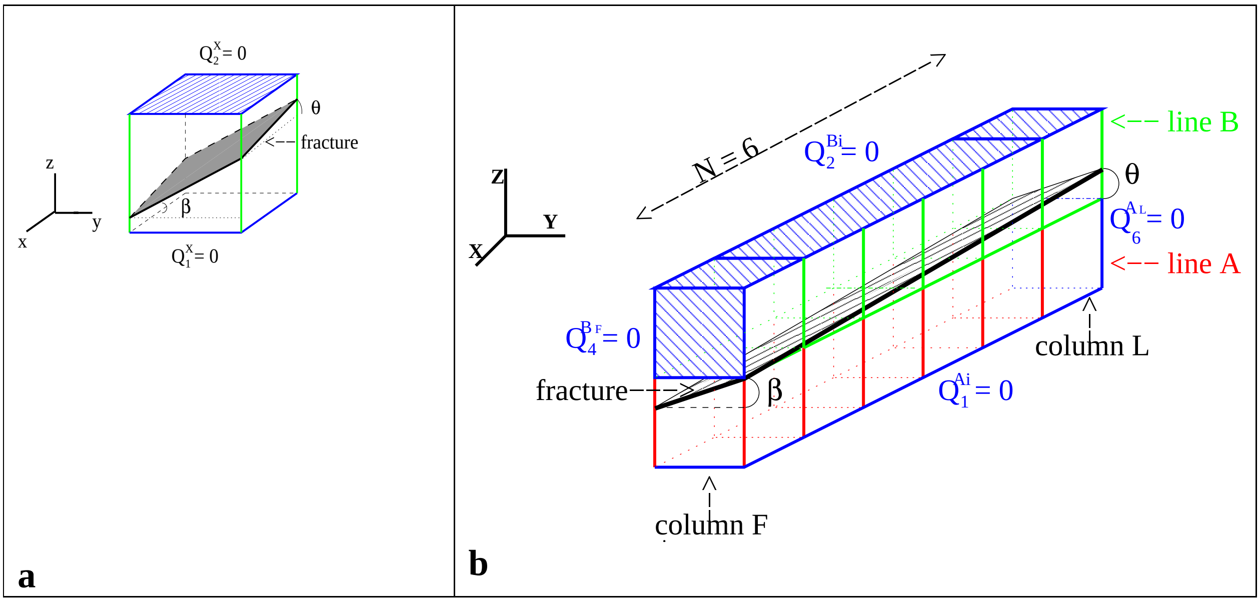

Fig. 3. Distinguishing between *S* and *C* set of cells according to the fracture location in the cells. a: Simple (*S*) set encloses neighbouring cells all in the same horizontal plane; b: Complex (*C*) set regrouping two lines of cells connecting two *S* sets.

3 Equivalent hydraulic conductivity computation

The approach for the computation of equivalent hydraulic conductivities is provided for the case of a single fracture. Section 3.1 presents the basic idea supporting the method as well as basic equations. The properties of the MHFE scheme essential for the approach are presented in Section 3.2. In Section 3.3, the equivalent properties are derived for $45° \ge \beta > \theta \ge 0°$ and extended to all geometries.

3-1 Introduction - a single fracture

As stated previously, the meshing of a fracture network is built using a regular grid. The geometry associated with a single fracture appears as a stair-shaped set of parallelepiped elements (see Figure 1 and Langevin, 2003; Hirano et al., 2010).

When modelling flow, the main concern is to evaluate the fluid flux occurring within the geometrical representation of the fracture and compare it with a "reference", the latter being analytical or stemming from a calculation over a very refined grid. For the problem of up-scaling hydraulic conductivity in a discretized fracture network as that discussed above, the question of fluid flux has to be handled at the scale of each grid cell. In the literature, a scalar value of hydraulic conductivity per grid cell is often used (Svensson, 2001a; Hirano et al. 2010). This choice may guarantee the flux conservation in 2-D cases (Fourno et al., 2007). Concerning 3-D problems, this section will show why the use of a scalar value can be a flawed assumption and how to upscale fracture hydraulic conductivity to correctly model the flux of a single fracture intersecting a single rectangular cuboid (see Figure 4, with L_X, L_Y, L_Z [L] the edge lengths of the cuboid).

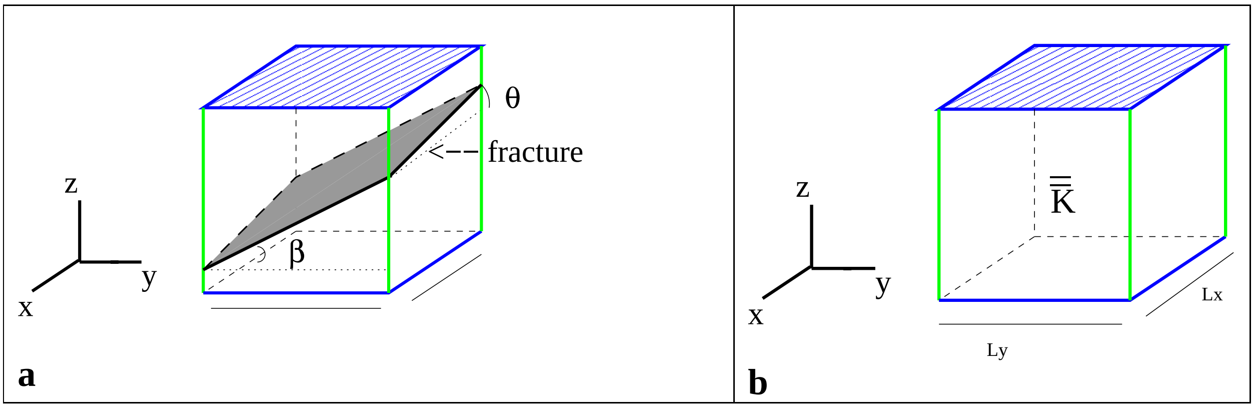

Fig. 4. A cell enclosing a portion of fracture (4a) and the equivalent hydraulic conductivity tensor associated with that cell (4b).

The fracture is modelled as a porous medium with a hydraulic conductivity, k [LT^{-1}] and an aperture a [L]. The fracture orientation is characterized by the angles θ and β. The fracture is not supposed to cross the top and bottom facets. The equations governing steady-state flow are classically the Darcy's equation (Eq. 1) and the mass balance equation (Eq. 2):

$$\vec{q} = -k.\vec{\nabla}h \qquad (1)$$

$$\vec{\nabla}.\vec{q} = s \qquad (2)$$

in which $\vec{q}$ [LT^{-1}] is the Darcy velocity, h [L] the head, s a source term [T^{-1}].

Considering the fracture position and orientation (Figure 4a), the boundary conditions of the rectangular cuboid intercepted by the fracture are of no flow type at the top and the bottom facets. Using a tensor notation, the classical analytical expression for the fluid flux, Q, is written as:

$$Q = \frac{ka}{c_n}\begin{bmatrix} \frac{\cos\theta}{\cos\beta}L_Y & \sin\beta.\sin\theta.L_Y & 0 \\ \sin\beta.\sin\theta.L_X & \frac{\cos\beta}{\cos\theta}L_X & 0 \\ 0 & 0 & 0 \end{bmatrix}\vec{\nabla}h \quad (3)$$

with $c_n = (1-\sin^2\beta\sin^2\theta)^{\frac{1}{2}}$.

For no flow boundary conditions at the top and bottom facets of the intersected parallelepiped element, the equivalent hydraulic conductivity tensor, $\overline{\overline{K}}$, can be calculated as:

$$\overline{\overline{K}} = \frac{ka}{c_n L_z}\begin{bmatrix} \frac{\cos\theta}{\cos\beta} & \sin\beta.\sin\theta & 0 \\ \sin\beta.\sin\theta & \frac{\cos\beta}{\cos\theta} & 0 \\ 0 & 0 & 0 \end{bmatrix} \quad (4)$$

Equation 4 demonstrates that the equivalent hydraulic conductivity has to be a tensor to correctly model the fracture flux magnitude and direction. Notably, when the opposite grid cell facets are not identical (as for unstructured meshing using the corner point grid technique) the hydraulic conductivity tensor is not symmetric.

In this paper, we propose to model fractures (and by extension fracture networks) using simplified diagonal hydraulic conductivity tensors. Considering that the off-diagonal elements of the tensor (Equation 4) depend on the product $\sin\beta\sin\theta$, the simplification into a diagonal tensor will be valid for values of β and/or θ close to zero. This geometrical configuration corresponds to sub-horizontal and sub-vertical fault networks. Equation 4 is obtained for specific flow boundary conditions of no-flow at the top and bottom facets; which contradicts the above statement of inferring diagonal tensors for sub-vertical fractures. Expressions similar to (4) can be obtained by permutations between directions *x*, *y*, and *z* so that to deal with sub-vertical fractures and flowing boundary conditions on the top and bottom facets (see Table 1 at the end of Section 3). At this stage of the paper, we focus the analysis on fractures honouring the condition $45° \geq \beta > \theta \geq 0°$ and decomposed into *S* or *C* subsets of cells (see Section 2). The equivalent permeability tensor is computed analytically thanks to MHFE properties (Section 3.2) for *S* and *C* groups of cells (Section 3.3).

3-2 Flow governing equation and MHFE scheme

The purpose of the present section is to provide the reader with some basic knowledge about the MHFE scheme. In particular, through the introduction of additional unknowns termed head traces, the water mass conservation principle can be formally established at the scale of a single cell or of a group of cells. This property is fundamental for the FCVA presented here and leads to the equivalent properties derived in the next Section. As previously introduced, our approach is based on diagonal hydraulic conductivity tensors. The steady-state flow equations (1) and (2) are rewritten in the form:

$$\vec{q} = -\overline{\overline{K}}^{set}\vec{\nabla}h \tag{5}$$

$$\vec{\nabla}.\vec{q} = s \tag{6}$$

with $\overline{\overline{K}}^{set}$ the diagonal hydraulic conductivity tensor [LT^{-1}]. In the following, the index "^{set}" will be replaced by ^{S} or ^{C} according to the *S* or *C* set of cells considered.

The goal is to relate equivalent hydraulic conductivity tensor components ($K_x^{set}, K_y^{set}, K_z^{set}$) to the fracture hydraulic conductivity, *k*. The numerical scheme used relies on mixed finite elements that preserve by construction the fluid fluxes normal to the interfaces between adjacent elements. To this end, specific variables are manipulated including the mean head $\overline{h}^E$ over an element *E* and the mean heads (also called traces) Th_i^E over the facet *i* of the element *E*. In the end, the elementary scheme involves 13 unknowns for a cubic element, i.e., 6 fluxes Q_i, 6 head traces Th_i and the mean head $\overline{h}^E$. Flow is calculated by handling the head traces as principal variables with the following form for fluxes and mean head (Mose et al., 1994; Dabbene et al., 1998; Bernard-Michel et al., 2004):

$$Q_i^E = \overline{h}_E \sum_j (M^{-1})_{ij}^E - \sum_j (M^{-1})_{ij}^E.(Th^{-1})_j^E \quad with \quad i = 1..6 \tag{7}$$

$$\overline{h}_E = \frac{\sum_i \alpha_i^E Th_i}{\sum_i \alpha_i^E} \tag{8}$$

with $\alpha_i^E = \sum_j (M^{-1})_{ij}^E$, $M_{ij}^E = \int_E (\vec{w}_i)^t (\overline{\overline{K}}^{set})^{-1} (\vec{w}_j) dE$, M^{-1} the inverse matrix of M and $\vec{w}_i$ defined as $\int_{F_j} \vec{w}_i . \vec{n} dF_j = \delta_{ij}$. Considering cubic elements (Δ^3) and diagonal hydraulic conductivity tensors, $\overline{\overline{K}}^{set}$, the hybrid mass matrix M^E writes:

$$M^E = \frac{1}{6\Delta} \begin{bmatrix} \frac{2}{K_z^{set}} & \frac{-1}{K_z^{set}} & 0 & 0 & 0 & 0 \\ \frac{-1}{K_z^{set}} & \frac{2}{K_z^{set}} & 0 & 0 & 0 & 0 \\ 0 & 0 & \frac{2}{K_y^{set}} & 0 & \frac{-1}{K_y^{set}} & 0 \\ 0 & 0 & 0 & \frac{2}{K_x^{set}} & 0 & \frac{-1}{K_x^{set}} \\ 0 & 0 & \frac{-1}{K_y^{set}} & 0 & \frac{2}{K_y^{set}} & 0 \\ 0 & 0 & 0 & \frac{-1}{K_x^{set}} & 0 & \frac{2}{K_x^{set}} \end{bmatrix} \tag{9}$$

Equation (7) can be easily written as

$$\overline{Q} = \overline{\overline{B}}_K \overline{T}_h \tag{10}$$

in which $\overline{\overline{B}}_K$ depends on values of fracture hydraulic conductivity.

Thanks to Equation (10), it is possible to associate numerical fluxes for a cubic discretization to an analytical flux whatever the head gradient. This means we are able to propose equivalent hydraulic conductivity tensors for *S* and *C* set of cells to obtain the exact flow occurring in a fracture.

3-3 Expression of fluxes with MHFE and derivation of equivalent hydraulic conductivities

By accounting for both the geometry of the modelled fractures and the MHFE numerical formalism, an analytical expression of the fluxes in each cell as a function of head gradients is obtained. Mass balance, head, head gradient and velocity are estimated within the element on the basis of the traces of heads along the facets of the element. Given the geometrical considerations reported in Figure 2, each element of the grid has a limited connectivity with its neighbours. This point is used to obtain the analytical expression of the MHFE fluxes. As mentioned earlier, the equivalent properties are computed for two types of cell groups for which no flow occurs through their top and bottom facets.

3-3-1 The S set of cells

In the case of cells from the *S* set (see Figures 3a and 4b), equations of MHFE fluxes are easy to obtain. With reference to facet notations reported in Figure 5, it can be noted that along the *x* direction, the unknown is $Q_x^S = Q_4^S = -Q_6^S$. By using Equation (10), it comes:

$$Q_x^S = -K_x^S.\Delta.\Delta h_x \quad \text{with} \quad \Delta h_x = Th_4 - Th_6 \tag{11}$$

Along the *y* direction, $Q_y^S = Q_5^S = -Q_3^S$ can be written as:

$$Q_y^S = -K_y^S.\Delta.\Delta h_y \quad \text{with} \quad \Delta h_y = Th_3 - Th_5 \tag{12}$$

For the set *S* of cells, the following equivalent hydraulic conductivity tensor ($\overline{\overline{K}}^S$) is obtained by flux conservation (see relations 3, 11 and 12):

$$\overline{\overline{K}}^S = \begin{bmatrix} K_x^S & 0 & 0 \\ 0 & K_y^S & 0 \\ 0 & 0 & K_z^S \end{bmatrix} \quad \textit{with} \quad \begin{array}{l} K_x^S = \dfrac{a}{\Delta}\dfrac{\cos\theta}{c_n \cos\beta}k \\ K_y^S = \dfrac{a}{\Delta}\dfrac{\cos\beta}{c_n \cos\theta}k \end{array} \tag{13}$$

Notably, K_z^S is not defined and can be set up at any value, for instance that of K_y^S

3-3-2 The C set of cells

The case of cells from the *C* set is trickier (Figures 3b and 5b). We denote by *A* and *B* the top and bottom lines of cells, respectively; the element A_i (respectively B_i) is the i$^{\text{th}}$ element of line *A* (respectively, line *B*) and Q_j^{Ai} is the flux through the facet *j* of the cell A_i (see Figure 5a for facet numbering).

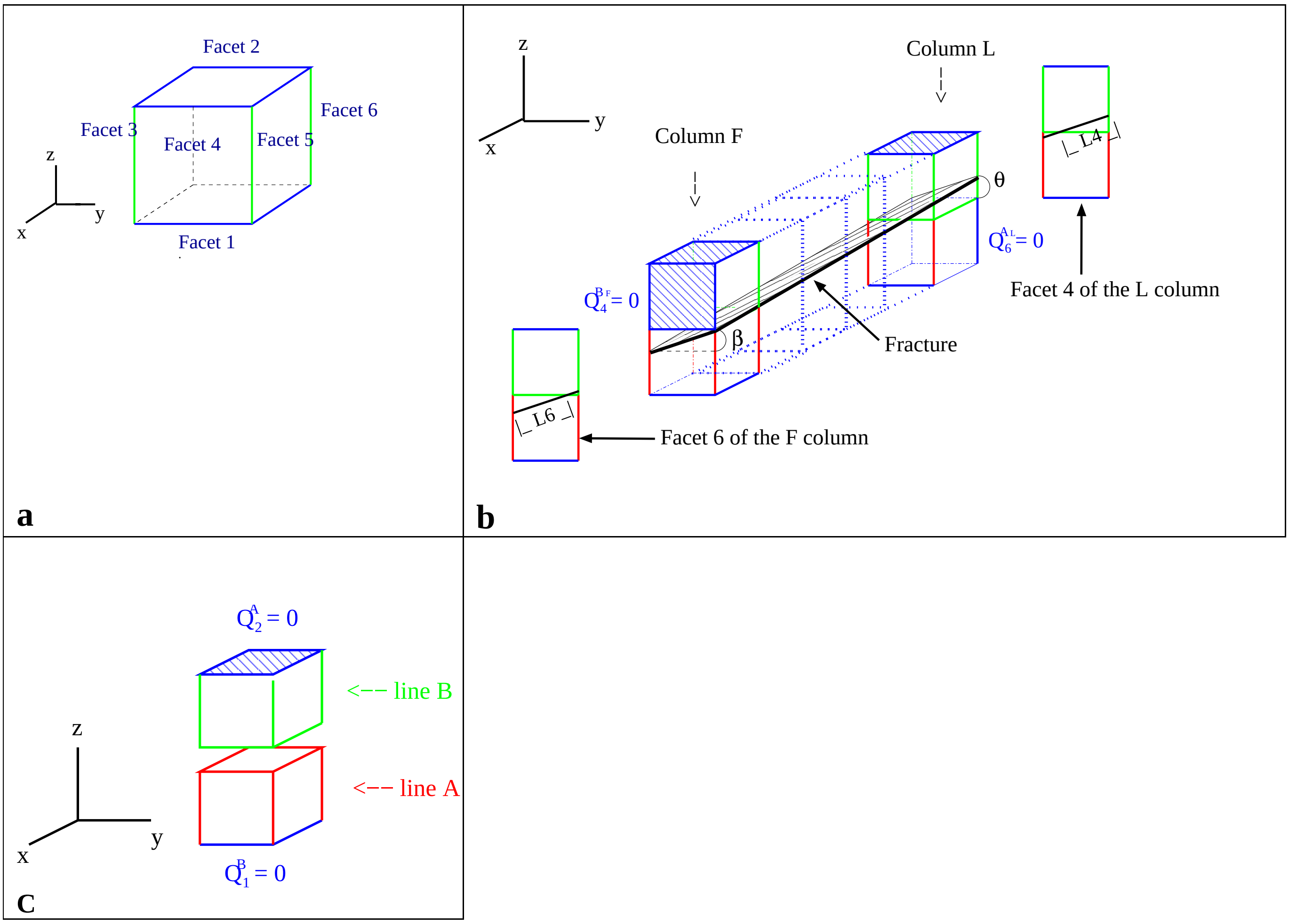

Fig. 5. a: facets numbering of a cubic mesh for flux calculations; b: fracture location in a set of 2*N* cells belonging to a complex (*C*) set of cells; c: two cells of a *C* set of cells (see Fig. 5b) with their local boundary conditions.

The following properties characterize the elements of the set *C*:

- Boundary conditions :

$$Q_1^{A_i} = Q_2^{B_i} = 0 \quad i = 0...N$$
$$Q_6^{A_N} = Q_4^{B_0} = 0 \qquad (14)$$

- Continuity conditions:

$$Q_6^{A_i} = Q_4^{A_{i+1}}$$
$$Q_6^{B_i} = Q_4^{B_{i+1}} \qquad (15)$$

- Geometrical conditions

N, the number of cells in a line of a C set, may be evaluated as a function of θ and β from the fracture position inside the C set (Figure 5b). We consider the intersections (traces) of the fracture with facet 4 of the first column of cells and facet 6 of the last (N^{th}) column of cells. We also assume that the two traces of fracture touch the horizontal plane separating the two lines of C cells, at the edge between facet 4 – facet 5 for the first column and the edge between facet 6 – facet 3 for the last column (see Figure 5). By denoting dz the variation of elevation of the traces on facets 4 and 6 mentioned above we note

$$\left|\tan\beta\right| = \frac{dz}{\Delta} \ , \ \left|\tan\theta\right| = \frac{dz}{N\Delta} \ \Rightarrow N = \frac{\left|\tan\beta\right|}{\left|\tan\theta\right|} \qquad (16)$$

It is obvious that the evaluation of N is an approximation because all the triplets (θ, β, Δ) do not allow an exact positioning of the fracture traces as assumed above. Usually, one may miss or add one cell compared with the real number of cells in a C set. Another observation is helpful. Considering the facet 6 of the first column (column F in Figure 5b) and the facet 4 of the last one (column L in Figure 5b), one can notice that the length $L6$ and $L4$ are equal yielding

$$Q_4^{A_N} = -Q_6^{B_0} \quad ; \quad Q_4^{B_N} = -Q_6^{A_0} \qquad (17)$$

The final relation deduced from geometrical observations is that describing how the flux crosses the last column (and by symmetry the first column too). Considering the facet 4 of the last column and the line A, the height variation of the fracture trace equals $dz = \Delta \tan\theta$. On this facet (facet 4, line A) the length of the fracture trace equals $L_4^A = \dfrac{dz}{\sin\beta}$ while the total length on the facet 4 (line A plus line B) is $L = \dfrac{\Delta}{\cos\beta}$. Knowing that $Q_4^{A_N} = Q_x^C \, L_4^A / L$, we obtain:

$$Q_4^{A_N} = \frac{\tan\theta}{\tan\beta} . Q_x^C \qquad (18)$$

A scalar value $U = \left|\dfrac{\tan\theta}{\tan\beta}\right|$ is introduced to simplify the previous relation $Q_4^{A_N} = U . Q_x^C$.

With the above conditions, we try now to express the flux in C set cells along the x and y directions Q_x^C, Q_y^C as functions of Δ, θ and β. Two directions of head gradients are applied onto the former systems to derive the associated flux along the same directions.

- *MHFE flux along the x direction*

Knowing that the hydraulic conductivity tensor of each element is diagonal, the following conditions can be expressed:

$$\begin{aligned} &Q_3^{A_i} = Q_3^{B_i} = 0 \quad i = 0...N \\ &Q_5^{A_i} = Q_5^{B_i} = 0 \quad i = 0...N \\ &Q_4^{A_0} = -Q_6^{B_N} = Q_x^C \end{aligned} \tag{19}$$

with Q_x^C the flux of C set along the x direction. Using the boundary, flow and geometrical conditions and Equation (10), the flow Q_x^C can be finally expressed as:

$$Q_x^C = -\frac{2\Delta K_x^C K_z^C}{\left(N+1-\frac{2U}{3}\right)K_z^C + \frac{4U}{3}K_x^C}\Delta h_x \tag{20}$$

Using the N and U values previously determined the final expression is obtained:

$$Q_x^C = -\frac{2\Delta K_x^C K_z^C}{\left(\left|\frac{\tan\beta}{\tan\theta}\right| + 1 - \frac{2\left|\frac{\tan\theta}{\tan\beta}\right|}{3}\right)K_z^C + \frac{4\left|\frac{\tan\theta}{\tan\beta}\right|}{3}K_x^C}\Delta h_x \tag{21}$$

- *MHFE flux along the y direction*

In the whole set C of cells, all the columns play the same role which allows simplifying the identification of fluxes along the y direction to the flux along a single column (Figure 5c). We note $\tilde{Q}_y^C$ the flux of a C set column along the y direction.

The flow boundary conditions are:

$$Q_4^A = Q_4^B = 0 \;\; ; \;\; Q_6^A = Q_6^B = 0 \;\; ; \;\; Q_5^B = -Q_3^A = \tilde{Q}_y^C \tag{22}$$

$\tilde{Q}_y^C$ is easily obtained by solving the following equations:

$$\begin{cases} Q_5^B - Q_3^A = 2Q_y^C \\ Q_2^B - Q_1^A = 0 \\ Q_3^B - Q_5^A = 0 \\ Q_4^B - Q_6^A = 0 \end{cases} \Rightarrow \tilde{Q}_y^C = -\frac{3}{2}\Delta \frac{K_y^C K_z^C}{K_y^C + K_z^C}\Delta h_y \tag{23}$$

For N columns of cells with $N = \left|\tan\beta / \tan\theta\right|$, the total flux Q_y^C along the y direction writes obviously:

$$Q_y^C = \left|\frac{\tan\beta}{\tan\theta}\right| . \tilde{Q}_y^C \tag{24}$$

- *Derivation of equivalent hydraulic conductivities*

Considering the relations, 3, 21, 23 and 24, the equivalent hydraulic conductivity tensor of C set cells can be written as:

$$\overline{\overline{K}}^C = \begin{bmatrix} K_x^C & 0 & 0 \\ 0 & K_y^C & 0 \\ 0 & 0 & K_z^C \end{bmatrix} \quad \textit{with} \quad \begin{array}{c} 2\dfrac{K_x^C K_z^C}{\left(1 + N - \dfrac{2}{3}U\right)K_z^C + \dfrac{4}{3}UK_x^C} = \dfrac{a}{\Delta N}\dfrac{\cos\theta}{c_n \cos\beta}k \\ \dfrac{3}{2}N\dfrac{K_y^C K_z^C}{K_y^C + K_z^C} = \dfrac{a}{\Delta}\dfrac{\cos\beta}{c_n \cos\theta}k \end{array} \tag{25}$$

With the assumption $K_z^C = K_y^C$, the following expressions are obtained:

$$\begin{array}{l} K_x^C = \dfrac{a}{\Delta}\dfrac{\cos\theta}{c_n \cos\beta}\dfrac{\left(1 + \left|\dfrac{\tan\theta}{\tan\beta}\right| - \dfrac{2}{3}\left(\dfrac{\tan\theta}{\tan\beta}\right)^2\right)}{\left(2 - \dfrac{\sin^2\theta}{\sin^2\beta}\right)}k \\ K_y^C = \dfrac{4}{3}\dfrac{a}{\Delta}\dfrac{\cos\beta}{c_n \cos\theta}k \end{array} \tag{26}$$

It is interesting to note that:

- the hydraulic conductivity tensor is established for $45° \geq \beta > \theta \geq 0°$ (Figures 5a, 5b),
- for the case $\beta = \theta = 0$, there are obviously only cells of S type and the classical correction $\dfrac{a}{\Delta}$ is obtained,
- for $\beta = \theta$, by symmetry $K_x^S = K_y^S$ *and* $K_x^C = K_y^C$.
-

The equivalent tensors can also be obtained for other fracture orientations by means of geometrical permutation between the *x*, *y* and *z* directions so that the former results are extended to all configurations. Considering the vector normal to the fracture plane, it is possible to switch the values of the equivalent tensor (by also changing the basis vector) and determine the values of θ and β with $45° \geq \beta > \theta \geq 0°$. The results are summed up in Table 1 in terms of equivalent tensor $\overline{\overline{K}}^{set}$.

	Configuration	**resulting tensor**	**configuration case**
1	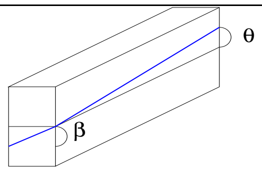	$\overline{\overline{K}}^{set} = \begin{bmatrix} K_x^{set} & 0 & 0 \\ 0 & K_y^{set} & 0 \\ 0 & 0 & K_z^{set} \end{bmatrix}$	$n_{\max} = n_z$ & $n_{\min} = n_y$ $\Rightarrow \beta = \arctan(\frac{n_x}{n_z})$, $\theta = \arctan(\frac{n_y}{n_z})$
2	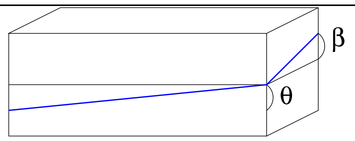	$\overline{\overline{K}}^{set} = \begin{bmatrix} K_y^{set} & 0 & 0 \\ 0 & K_x^{set} & 0 \\ 0 & 0 & K_z^{set} \end{bmatrix}$	$n_{\max} = n_z$ & $n_{\min} = n_x$ $\Rightarrow \beta = \arctan(\frac{n_y}{n_z})$, $\theta = \arctan(\frac{n_x}{n_z})$
3	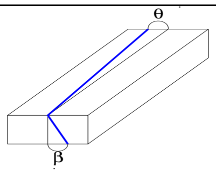	$\overline{\overline{K}}^{set} = \begin{bmatrix} K_x^{set} & 0 & 0 \\ 0 & K_z^{set} & 0 \\ 0 & 0 & K_y^{set} \end{bmatrix}$	$n_{\max} = n_y$ & $n_{\min} = n_z$ $\Rightarrow \beta = \arctan(\frac{n_x}{n_y})$, $\theta = \arctan(\frac{n_z}{n_y})$
4	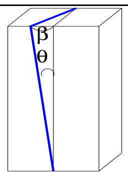	$\overline{\overline{K}}^{set} = \begin{bmatrix} K_y^{set} & 0 & 0 \\ 0 & K_z^{set} & 0 \\ 0 & 0 & K_x^{set} \end{bmatrix}$	$n_{\max} = n_y$ & $n_{\min} = n_x$ $\Rightarrow \beta = \arctan(\frac{n_z}{n_y})$, $\theta = \arctan(\frac{n_x}{n_y})$
5	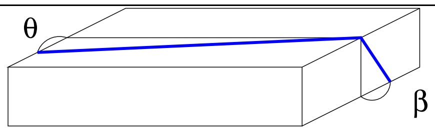	$\overline{\overline{K}}^{set} = \begin{bmatrix} K_z^{set} & 0 & 0 \\ 0 & K_x^{set} & 0 \\ 0 & 0 & K_y^{set} \end{bmatrix}$	$n_{\max} = n_x$ & $n_{\min} = n_z$ $\Rightarrow \beta = \arctan(\frac{n_y}{n_x})$, $\theta = \arctan(\frac{n_z}{n_x})$
6	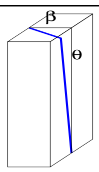	$\overline{\overline{K}}^{set} = \begin{bmatrix} K_z^{set} & 0 & 0 \\ 0 & K_y^{set} & 0 \\ 0 & 0 & K_x^{set} \end{bmatrix}$	$n_{\max} = n_x$ & $n_{\min} = n_y$ $\Rightarrow \beta = \arctan(\frac{n_z}{n_x})$, $\theta = \arctan(\frac{n_y}{n_x})$

Table 1. How to correctly orientate the equivalent tensor according to the fracture orientation. θ (respectively, β) is the angle between the horizontal plane *x*-*y* and the fracture intersection (trace) on the vertical plane *x*-*z* (respectively, *y*-*z*)

4 Evaluation of equivalent properties

The FCVA is now tested against analytical results for flow: 1- in a single fracture with various dips and strikes, and 2- in regular fracture networks. As already mentioned, the equivalent (full) tensor is diagonal. The approximation is strictly valid for sub-vertical or sub-horizontal fractures. The non-diagonal components increase as a function of $\sin\beta\sin\theta$. For all configurations, the hydraulic conductivity of the fracture(s) is 3.8×10^{-8} m.s^{-1} (= 4 darcys), the fracture aperture is 2.10^{-2} m. In Section 4.2, the case of fracture networks is considered with emphasis on the specific issue of fracture intersections.

4-1 Sensitivity to the orientation for flow in a single fracture

The fracture crosses the regular grid from one side to the opposite side. Different dip and strike configurations are tested. For each mesh direction, i = x, y, z, the breakthrough flux, Q^{i}_{num} is calculated using the MHFE voxel approach. An analytical expression of this flux Q^{i}_{ana} is also obtained considering Equation (3) and for which L_X, L_Y, L_Z are now the medium lengths. For each fracture orientation, both analytical and numerical up-scaled hydraulic conductivity tensors are derived from fluxes. The diagonalized "numerical" tensor $K_n^{ups,num}$ resulting from the FCVA is compared with the analytical one $K_n^{ups,ana}$ and a relative error is defined as the ratio $\frac{\left|K_n^{ups,num} - K_n^{ups,ana}\right|}{K_n^{ups,ana}}$ with the index n referring to the minimal, intermediate and maximal value of the tensor components. Table 2 summarizes the results for the different fracture orientations.

Error on $\begin{bmatrix} k_{\min} \\ k_{\text{int}} \\ k_{\max} \end{bmatrix}$ (%)		θ (°)			
β ,(°)		0.	15.	30	45.
	0.	$\begin{bmatrix} 0. \\ 0. \\ 0. \end{bmatrix}$	$\begin{bmatrix} 0. \\ 0.6 \\ 0. \end{bmatrix}$	$\begin{bmatrix} 0. \\ 2.8 \\ 0. \end{bmatrix}$	$\begin{bmatrix} 0. \\ 13.8 \\ 0. \end{bmatrix}$
	10.	$\begin{bmatrix} 0. \\ 0.2 \\ 0. \end{bmatrix}$	$\begin{bmatrix} 0. \\ 1.1 \\ 8.7 \end{bmatrix}$	$\begin{bmatrix} 0. \\ 5.1 \\ 4.4 \end{bmatrix}$	$\begin{bmatrix} 0. \\ 15.2 \\ 3.7 \end{bmatrix}$
	20.	$\begin{bmatrix} 0. \\ 1.6 \\ 0. \end{bmatrix}$	$\begin{bmatrix} 0. \\ 1.9 \\ 11. \end{bmatrix}$	$\begin{bmatrix} 0. \\ 8.5 \\ 9.2 \end{bmatrix}$	$\begin{bmatrix} 0. \\ 24.2 \\ 13.9 \end{bmatrix}$
	30.	$\begin{bmatrix} 0. \\ 1.0 \\ 0. \end{bmatrix}$	$\begin{bmatrix} 0. \\ 7.2 \\ 5.9 \end{bmatrix}$	$\begin{bmatrix} 0. \\ 12.6 \\ 20.3 \end{bmatrix}$	$\begin{bmatrix} 0. \\ 22.4 \\ 11.9 \end{bmatrix}$

Table 2. Errors on equivalent tensor of hydraulic conductivity between FCVA and analytical values for the cases of a single fracture with different orientations. θ (respectively, β) is the angle between the horizontal plane *x-y* and the fracture intersection (trace) on the vertical plane *x-z* (respectively, *y-z*)

Four points can be extracted from Table 2.

1. For $\theta = 0$ and $\beta = 0$, the local hydraulic conductivity of the fracture is simply corrected by the ratio $\frac{a}{\Delta}$ and exact fluxes are obtained by construction (i.e., null error in Table 2).
2. Equation 4 shows that for the values ($\theta = 0$ and $\beta \neq 0$) or ($\theta \neq 0$ and $\beta = 0$) the analytical hydraulic conductivity tensor is diagonal as is also the case for the numerical tensors of the *S* and *C* cell sets of the FCVA. The consequence is that for configurations in which one of the angles θ or β is null, the flux directions are perfectly modelled and errors are of only a few percent.
3. For other fracture orientations, precision depends on the value of $\sin\beta\sin\theta$ (see Eq (3)). When considering diagonal hydraulic conductivity tensor in the voxel approach, the non-

diagonal flux values (Eq (2)) are supposed to be negligible. This is not always the case and the larger the value of $\sin\beta\sin\theta$, the larger the errors become.

This test case confirms that the equivalent properties are exact for fractures aligned with a main grid direction. The error increases when fracture orientations deviate from such conditions. The maximum error is less than 30%. For a real case study, when feasible, a main axis as close as possible to the fracture plane orientations should be chosen.

4-2 Hydraulic conductivity of regular fracture networks

The second case study is that of a regular fracture network in a block of $100\times100\times8$ m^3. The system is not strictly three-dimensional because fractures are vertical and main hydraulic gradients in the block concealing the fracture network are horizontal. These settings, however, allow a better assessment of the influence of fracture intersections. We first show that some constraints in terms of grid size exist to actually represent the connectivity of the fracture network on a regular grid. The smaller the grid size, the closer the representation is to the geometrical reality. The contact surface between two intersecting fractures obviously depends on the size of the mesh, so that head gradients as well as flux exchanged across the intersection should intuitively depend upon the grid size. The convergence of the flux in the network toward a constant value with grid size is reached for cell dimensions tending to the fracture aperture.

The fracture network (Figure 6) is made of four families of vertical fractures with directions of 10°, 34.5°, 100°, and 124.5° (Figure 7). The network is mapped onto five regular grids with meshes varying from 0.1 m on a side up to 4 m (Figures 6a, 6c). For the purpose of comparison, the network is also explicitly meshed (without mapping). No special effort to optimize the number of cells was done for this explicit meshing and both fracture planes and fracture intersections are discretized at a mean cell size of 0.2 m (Figure 6b). With the network topology and the explicit meshing, the modelling exercise is very similar to that depicted in Karimi-Fard et al. (2006). This exercise will also serve as reference for evaluating accuracy of fluxes draw from the FCVA approach. The properties associated with the fractures of all families are constant: hydraulic conductivity (3.8×10^{-8} m.s^{-1}) and aperture (2.10^{-2} m). Figure 6 shows the same fracture network mapped onto two regular grids, the first with a fine space step (0.2 m, Figure 6a), the second with a coarse step (4 m, Figure 6c). In the second case, the connectivity of the system is not represented. The contact surface at the fracture intersections is better modelled for the finest grid. The validation of the FCVA is addressed by considering numerical fluxes from FCVA, analytical fluxes from (3) and numerical fluxes from the explicit meshing of the fracture network. We note $Q_{i\,j}$ the flux through the facet j (or equivalently along direction j) considering a head gradient along the direction i. The specific label $Q_{i\,j}^{expl}$ denotes fluxes from the explicit meshing of the network. Using Equation 3, analytical fluxes of the whole network $Q_{i\,j}^{ana}$ are calculated as the sum of analytical fluxes associated with the individual fractures.

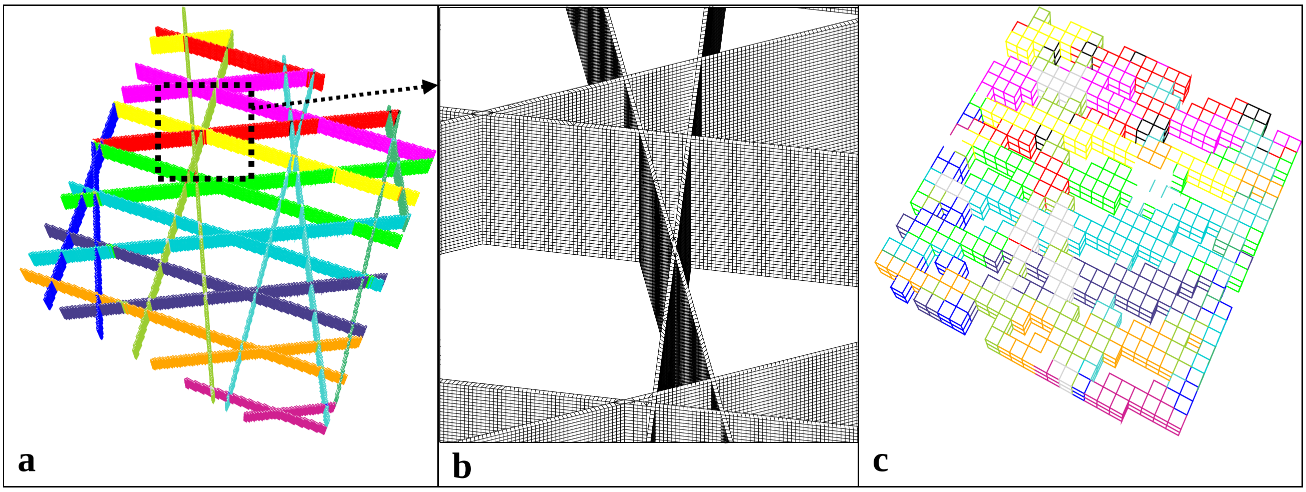

Fig. 6. Discretization of a regular fracture network by using a fine grid size of 0.2 m on a side (a) and a coarse grid size of 4 m (c). In b a portion of the explicit meshing of the fracture network for the purpose of comparison with the mapping procedure.

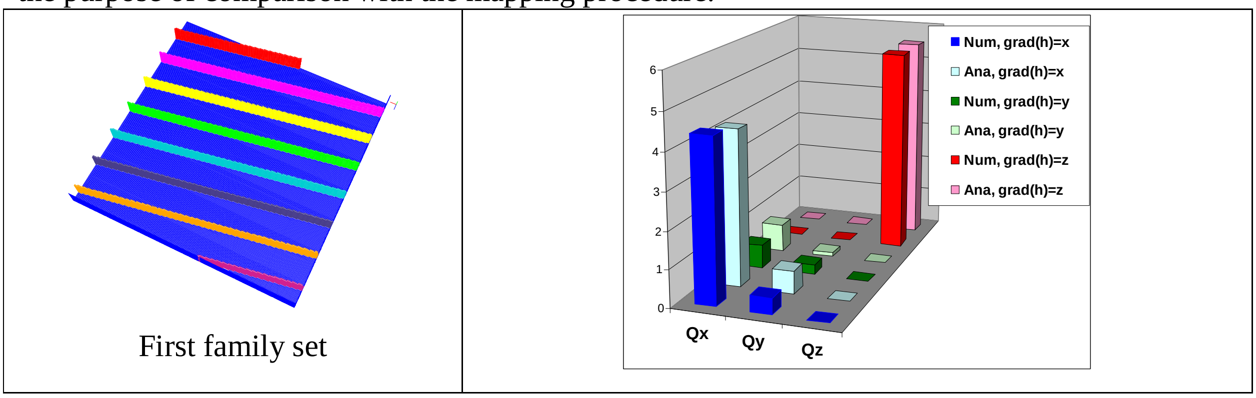

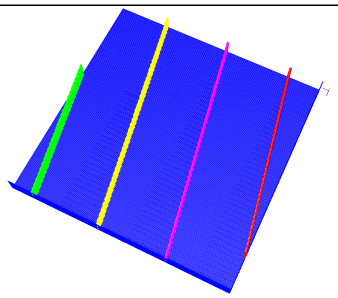

Second family set

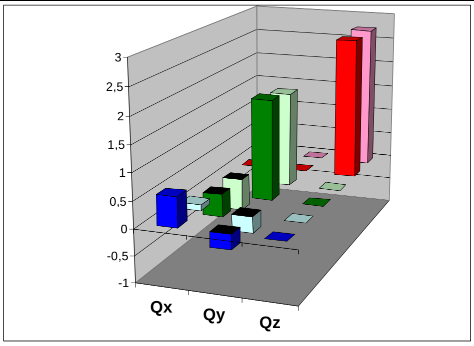

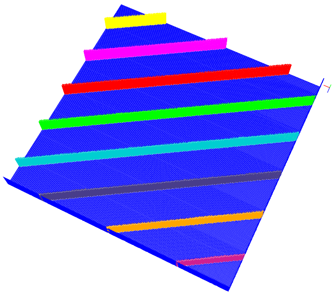

Third family set

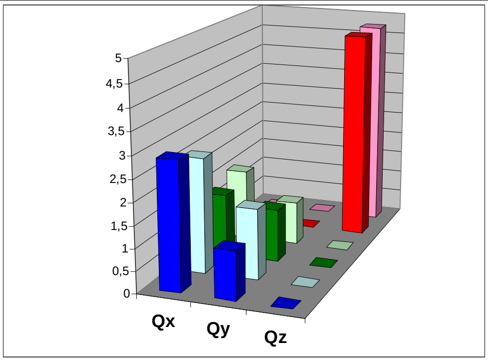

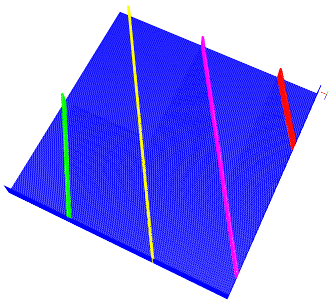

Fourth family set

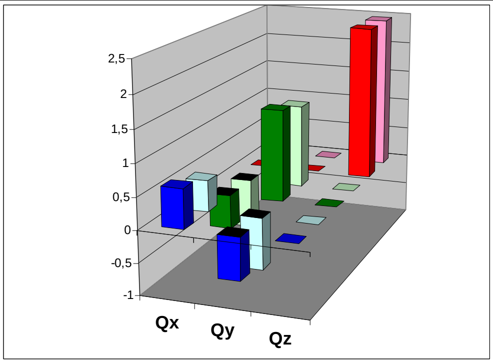

Fig. 7. Calculations of fluxes in a block enclosing different families of parallel fractures. Q_x, Q_y, and Q_z refer to the fluxes in the whole block along the *x*, *y* and *z* directions, respectively. Labels "*Ana*" and "*Num*" refer to analytical solutions and numerical ones. The fluxes Q_x, Q_y and Q_z are calculated for three main head gradients along the *x*, *y* and *z* directions.

In a first stage, we study the fluxes in each of the four fracture families of the fracture network independently (Figure 7). This is done in order to compare FCVA numerical flux values with analytical ones. The error should be stronger than for the single fracture test case because there is a side effect for the fractures which cross the fractured block from a vertical facet to a vertical adjacent one. Indeed, for these fractures, the no-flow boundary condition is not respected for the *S* and *C* sets of cells that touch the sides of the block. The fluxes through each facet of the fractured block are reported in Figure 7 considering three head gradient directions. As expected, the flow is correctly modelled for each fracture set. The order of magnitude of the different fluxes is well captured, with relative errors between analytical and numerical fluxes less than 10%.

In a second stage, we model flow into the whole network including the four fracture families. This exercise is performed by assigning the fracture intersection with the highest hydraulic conductivity value of the fractures present at the intersection. The analytical fluxes are still obtained as the sum of fluxes in each fracture (drawn from Equation 3). The above settings correspond to the classical approach of Oda (1986) which, in terms of fracture intersections, is equivalent to assume independent flow between fractures. If the same strategy is applied to numerical fluxes (i.e., by summing the numerical fluxes of each fracture family), it is obvious that the total numerical fluxes will be similar to analytical ones simply because FCVA is accurate for poorly connected fracture networks. On the other hand, calculating flux over the whole network, including interactions between fractures at their intersections, will cause the numerical fluxes to diverge from analytical ones. First, we note that the numerical fluxes calculated from a network explicitly meshed at small mesh size (see above) are similar to that from the analytical ones. This is the consequence of the explicit and precise meshing of fracture intersections to which the highest local hydraulic conductivities are assigned. In addition there is no dead-ends in the fracture network. No forces (except the local conductivity) are opposed to flow in each fracture with the consequence that the total flux in the block is the mere addition of each fracture contribution. In the end, the differences between FCVA and analytical (or explicit meshing) approaches must be associated with the FCVA geometrical representation of the fracture network and depend on the discretization. Figures 8 and 9 report on analytical fluxes, numerical fluxes from an explicit meshing of the network and FCVA fluxes values of the fractured block for different mesh size values (from 0.1 to 4 m).

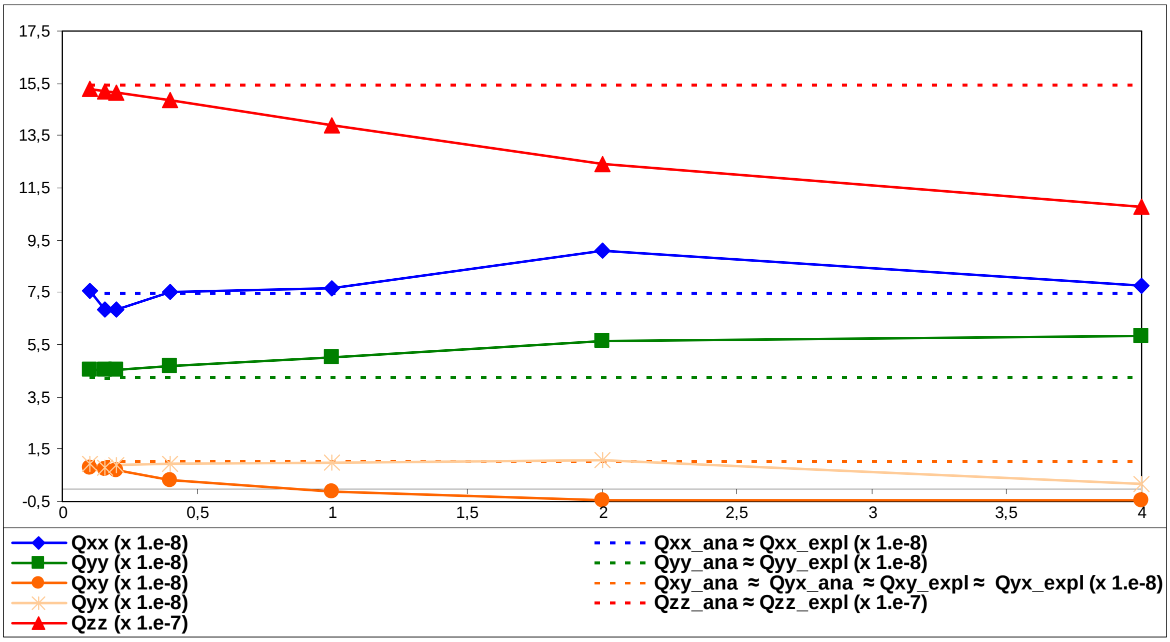

Fig. 8. Evolution of calculated fluxes in a fractured block (network in Fig. 6) with elementary mesh sizes evolving from 0.1 to 4 m on a side. The notation Q_{ij} ($i, j = x, y, z$) refers to fluxes along the *j* direction for a main head gradient along the *i* direction. The analytical values "*Ana*" are that from the Oda's assumption stating independent flow between fractures. The values labelled "Expl" stem from calculation over a fracture network explicitly (completely) meshed for both fracture planes and fracture intersections.

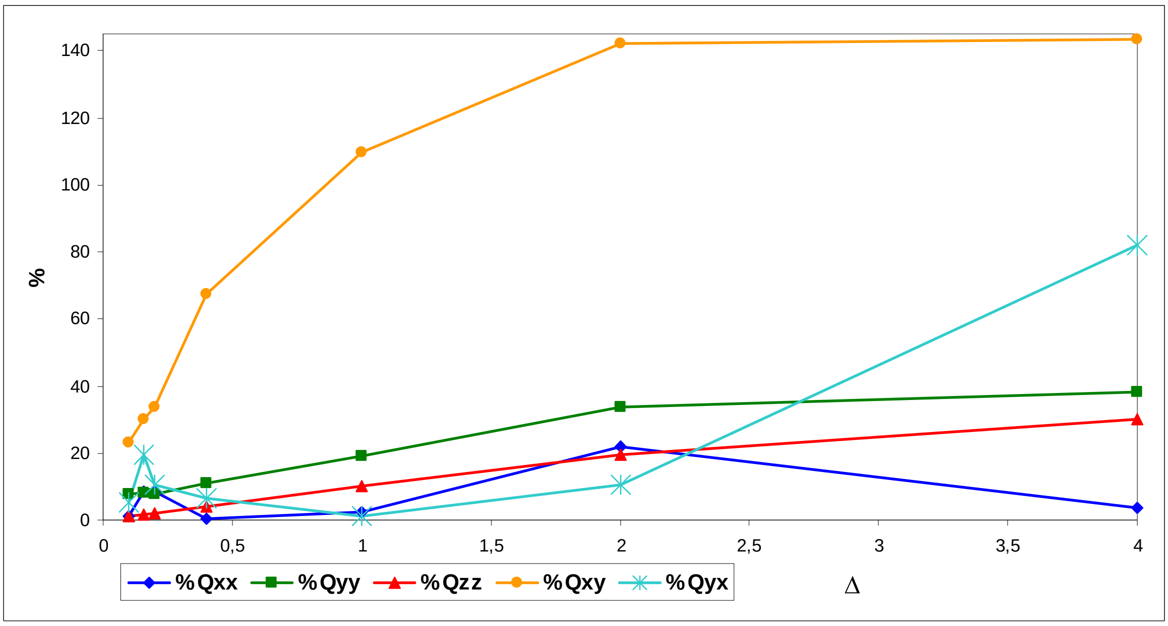

Fig. 9. Fluxes through a fractured block (network in Fig. 6). Evolution of the relative error (Q_{num} – Q_{ana})/Q_{ana} with elementary mesh sizes in the range 0.1 – 4 m. Q_{ij} ($i, j = x, y, z$) refers to fluxes along the *j* direction for a main head gradient along the *i* direction.

The main observation is a convergence of FCVA numerical fluxes values toward analytical ones when decreasing the mesh size. For finer grids (mesh size values of 0.1 – 1 m), the relative error on fluxes is close to 10 %, which is generally very reasonable in view of the weak precision on hydraulic property measurements in natural media. When increasing the mesh size, the evolution of relative errors on fluxes is not monotonic (Figure 9), especially for marginal fluxes Q_{ij}, i.e., fluxes along direction i when applying a main head gradient along direction j, $j \neq i$. Relative errors may reach 50-100% on Q_{ij} $j \neq i$ but theses fluxes are also ten times less than fluxes Q_{ii} making therefore a relative error of 50% on Q_{ij}, something small compared to the total flux conveyed by the fractures. The non-monotonic behaviour of errors comes from the competition between: 1- the calculation of the number N of cells in a "Complex" C set (cells connecting by their horizontal facets two portions of planes of different elevation); 2- some cells at the limits of the fractured block may show non-null fluxes through their top and bottom facets, which contradicts the assumption used to calculate hydraulic conductivity tensors (see Section 3). As expected however, for coarse discretizations with rough representations of fracture intersections, the general trend is that of errors on equivalent conductivity tensors increasing quickly with the discretization size. The first criterion for providing accurate results is to respect the connectivity of the fracture network; as a rule of thumb, the smallest matrix block between fractures should be represented by a few cells. However, by considering the order of magnitude of errors with reference to computation efforts, simulations based on coarse discretizations may be very attractive for preliminary results. These computations efforts are summed up in Table 3 for different FCVA discretizations.

Δ (m)	Number of cells	Meshing CPU time (s)	Flow (3directions) CPU time (s)
4	884	3	1
2	4108	7	6
1	18240	24	34
0.4	121440	193	370
0.2	495120	864	23257

Table 3. Computation times for meshing and calculating fluxes over a fracture network (network in Fig. 6) at different cell sizes.

In a final exercise, flow simulations are performed for different assumptions regarding the behaviour of fracture intersections. The goal is not to propose a third validation exercise of the FCVA but to illustrate how an additional freedom degree can be added in modelling flow by introducing different hydraulic behaviours at fracture intersections. Ideally, the choice of intersection modelling should be dictated by geological considerations. In practice, the values of hydraulic conductivity at fracture intersections could have some statistical dependence on the values of intercepting fractures, or be in a range of values supposed to mimic a set of objects between clogged and widely opened intersections. Four intersection models are considered in the following sensitivity study. A first choice is to assign, at the intersection cells, the highest hydraulic conductivity of intersecting fractures and correct it to obtain the equivalent permeability tensor (Model I1, already used in the previous simulations). Another option (model I2) is to sum each fracture contribution and to correct the obtained value. These choices do not significantly change the order of magnitude of hydraulic conductivity values applied to the intersection cells. Thus, to model extreme cases as clogged or opened intersections, we apply a correction to the highest hydraulic conductivity value of fractures present at the intersection (i.e., corrections to I1), respectively $k_{\text{int}}^{cor} = \frac{a}{\Delta}10^{-6}$ for a clogged intersection (model I3a) or $k_{\text{int}}^{cor} = 10\frac{a}{\Delta}$ for an opened intersection (model I3b).

The influence of these models I1 to I3b is studied for the network of four fracture families discussed above and discretized at the constant grid size of 0.4 m. The incidences in terms of breakthrough fluxes through the facets of the fractured block are illustrated in Figure 10.

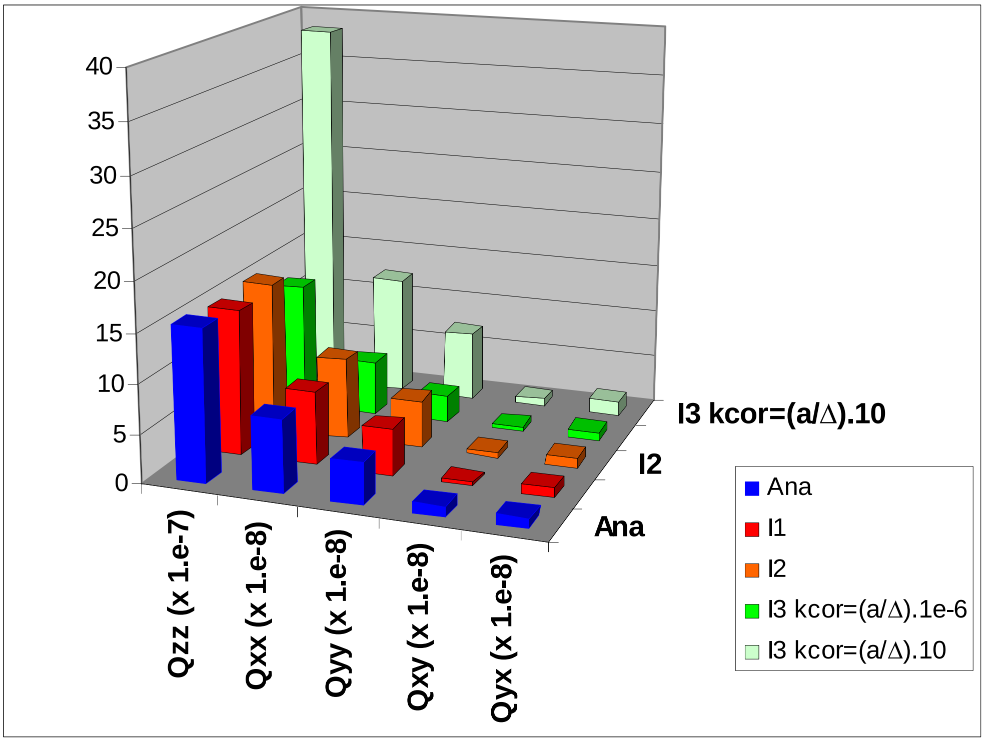

Fig. 10. Sensitivity of fluxes through a fractured block (network in Fig. 6) to the various choices of hydraulic conductivity tensors at fracture intersections (Q_{ij} is the flux along the direction *j* considering a head gradient along the direction *i*). "*Ana*" corresponds to analytical solution. I1: intersections with the highest conductivity of intersecting fractures; I2: intersections summing each fracture contribution; I3a: "clogged" intersection; I3b: "opened" intersection.

The analytical expressions corresponding to Oda's conditions are used as a reference for comparison purposes. As stated before, this reference considers no interactions between fractures leading to a full hydraulic conductivity tensor. Relative discrepancies on fluxes Q_{xx}, Q_{yy}, Q_{zz} (Q_{ij} stands for flux through facet *j* for a head gradient along *i*) between the analytical Oda's case and the numerical results are computed. The relative errors $\left(Q^{num} - Q^{ana}\right) / Q^{ana}$ are on average of (0.2%, 11%, 4%), (11%, 15%, 1%), (26%, 33%, 16%) and (62%, 69%, 148%) for models I1, I2, I3a and I3b, respectively. Models I1 and I2 (with hydraulic conductivity tensors assigned to intersections of the same order of magnitude as that of fractures) lead to comparable results in terms of fluxes. This is not the case for models I3a and I3b, in which the order of magnitude of hydraulic conductivity tensors of fracture intersections significantly differs from the fracture hydraulic conductivity. Notably, it could be expected from the I3a case, corresponding to very low permeability at intersections, that it renders the largest differences between analytical and numerical fluxes. Actually, this is not the case here because of the type of boundary conditions used (linear variation of heads along the contours of the block), allowing preferential flow along the sides of the block when it is hard to pass through the block because of clogged fracture intersections. In the end and at least for the three models of intersections I1, I2 and I3a, it seems that the behaviour of fracture intersections does not significantly modify the macroscopic hydraulic conductivity of the whole fractured block.

5 Conclusions

This paper proposes a new voxel continuum approach for fractured media (FCVA, Fracture Continuum Voxel Approach) as part of a general modelling strategy which consists in mapping main fractures onto a regular three-dimensional grid while minor fractures and matrix blocks are represented by an equivalent porous medium (of single or dual porosity). FCVA put emphasis on calculating equivalent hydraulic conductivity tensors, as opposed to scalar values, for regular cells discretizing the fracture network.

The voxel continuum approach is developed for planar fractures. The method requires a preliminary step of choosing the right cell size for mapping the fracture network. The cell size should keep the fracture network connectivity with a minimum amount of cells. The second step provides equivalent conductivity values of these cells in the general framework of a Mixed Hybrid Finite Element (MHFE) scheme for solving Darcian flow and preserving fluid fluxes at the interfaces between elements. This approach presents the advantages of providing a much localized fracture geometry and equivalent properties in terms of tensors instead of scalar values (e.g., compared with smeared fracture approaches). However and for the sake of simplicity and computational efficiency: 1- the tensors are calculated for groups of cells with the same geometric configuration and hydraulic behaviour in the fracture plane, and 2- the tensors are limited to their diagonal terms.

Applicability of FCVA for steady-state Darcian flow was evaluated on test cases handling both single fractures and fracture networks. For single fractures, the error in terms of flux values is limited to 25% for the worst case of fracture azimuth and dip close to 45°. For fracture networks, alignment of fracture planes with the main directions of the discrete grid allows to minimize errors on fluxes (and hydraulic conductivity tensors). The optimal case is obtained for networks composed of sub-vertical and sub-horizontal families (error of a few per cents). Such levels of errors are reasonable as compared to classical uncertainties obtained when measuring hydraulic properties of natural fractures. Still, for fracture networks, a minimal network dependent grid size is required to accurately represent the geometry and connectivity of the system. As a rule of thumb, the minimal size of matrix blocks between fractures should be discretized by a few grid cells (2-4). For smaller grid sizes, the accuracy of the flow simulation increases. Depending on the given application, the user may then balance accuracy versus computational effort.

Another issue is the treatment of fracture intersections in fracture networks. The approach by Oda (1986), though precise (full tensor), makes strong assumptions on the equivalent hydraulic behaviour of a fractured block in adding the contributions of all fractures (equivalent to state the independence of flow between all intercepting fractures). The FCVA voxel continuum approach allows various assumptions for assigning hydraulic conductivity of fracture intersections. In all cases it is important to note that a user can improve the effective hydraulic conductivity of the whole fractured block by changing conductivities at intersections.

Perspectives in the near future will address the problem of heterogeneous properties within each fracture plane. Because cells in a fracture plane are regrouped into so-called *S* and *C* subsets, it is envisioned that further versions of FCVA will handle uniform properties of cells within a given group, but varying between different *S* and *C* groups of the same discretized fracture plane. Notably, the extension of FCVA to other objects than planar fractures is also under study. Some of them, such as bounded rectangles or squares, disk or ellipsoid shaped planes, could be handled directly by starting with an infinite fracture plane intersecting the whole domain and then removing the grid cells that do not belong to the prescribed geometry. Other types of objects, like wells, tunnels etc., require more algorithmic efforts. We also raise that modelling flow at fracture intersections should be improved in terms of tensor representation and flux distribution. The theory and parameters that define a flow dimension could be investigated and used to quantify flow magnitudes distributions consistent with fracture connectivity (Barker 1991; Geier et al., 1996; Andra 2001). This might become an important issue especially if FCVA is envisioned as a possible tool for solute transport modelling.

Finally, we note that the development of meshing tools based on corner-point grids and non-structured finite-volume approaches to discretize flow equations are also very appealing. They allow meshing objects of complex geometry (including warped fracture planes and their relationship with the host matrix) with a reasonable number of cells. The finite-volume (control volume) approach is a priori incompatible with the MHFE technique because mass conservation in finite-volumes is associated with (harmonic) averaging of conduction properties between adjacent elements. MHFE do not rely on averaging, each finite element keeping its own hydraulic properties. Mass conservation is fulfilled in building the discrete system of equations by equating inlet-outlet fluxes at the interfaces between adjacent elements. Except for this technical point, the FCVA and its calculation of anisotropic tensors are not banned from applications to non-structured meshing. We foresee some possibilities to map fractures onto corner-point grids. These possibilities assume: 1- to build an algorithm able to remove useless cells at intersections juxtaposing pieces of planar objects representing the fractures (see Section 3), 2- to calculate MHFE fluxes over contorted elements. This is feasible especially with a variation of MHFE handling a single unknown per element (Younes et al., 2010). With this variation, MHFE adopt a philosophy very similar to control-volumes while avoiding calculations of inter-block parameters. The latter feature would facilitate the evaluation of full anisotropic tensors of hydraulic conductivity. Nevertheless, adapting the mapping presented in this paper to corner-point gridding needs for important algorithmic efforts that are postponed to further investigations.

References

Adler, P-M., Mourzenko, V.V., Thovert, J-F., Bogdanov, I., 2005. Study of single and multiphase flow in fractured porous media, using a percolation approach. International Symposium on Dynamics of Fluids in Fractured Rock, No2, Berkeley, CA, USA, 162, 33-41.

Andra 2001, Interpretation of well-tests in fractured media with flow dimension approach. Rapport Andra n° DRPOITA.00-29A.

Barker, J. A., 1991. The reciprocity principle and an analytical solution for Darcian flow in a network. Water Resour. Res. 27 (5) 743-746.

Barrenblatt, G., Zheltov, I., Kochina, I., 1960. Basic concepts in the theory of seepage of homogeneous liquids in fissured rocks. J. Appl. Math. Mech. 24, 852-864.

Bear, J., Tsang, C.F., de Marsily, G., 1993. Flow and contaminant transport in fractured rock. Academic Press, San Diego, CA, USA, 560 pp.

Berkowitz, B., 2002. Characterizing flow and transport in fractured geological media: A review. Adv. Water Resour. 25 (8), 861-884.

Bernard-Michel, G., Le Potier, G.C., Beccantini, A., Gounand, S., Chraibi, M., 2004. The Andra Couplex 1 Test CaseÂ : Comparisons between finite-element, mixed hybrid finite element and finite volume element discretizations. Comput. Geosc. 8 (2), 187-201.

Bogdanov, I., Mourzenko, V.V., Thovert, J-F., Adler, P-M., 2003. Two-phase flow through fractured porous media. Phys. Rev. E 68, 026703.

Bourbiaux, B., 2010. Fractured reservoir simulation: A challenging and rewarding issue. Oil Gas Sci. and Technol. 65 (2), 227-238.

Bourbiaux, B., Cacas, M.C., Sarda, S., Sabathier, J6C., 1998. A rapid and efficient methodology to convert fractured reservoir images into a dual porosity model. Rev. IFP, 53 (6), 785-799.

Cacas, M.C., Ledoux, E., de Marsily, G.,Tillie, B., Barbreau, A., Durand, E., Feuga, B., Peaudecerf, P., 1990. Modeling fracture flow with a stochastic discrete fracture network: calibration and validation: 1. The flow model, Water Resour. Res. 26 (3), 479-489.

Chapman, N., McCombie, C., 2003. Principles and standards for the disposal of long-lived radioactive wastes. Waste Management Series. Elsevier, Amsterdam, The Netherlands, 292 pp.

Cast3M, 2009. Web site for computer code Cast3M available at www-cast3m.cea.fr.

Cvetkovic, V., Painter, S., Outters, N., Selroos, J.O., 2004. Stochastic simulation of radionuclide migration in discretely fractured rock near the Aspo hard rock laboratory. Water Resour. Res. 40, W02404.

Dabbene, F., Paillere, H., Magnaud, J-P., 1998. Mixed Hybrid Finite Elements for transport of pollutants by underground water. Proc.10th Conference on Finite Elements in Fluids, Tucson, AZ, USA.

De Dreuzy, J-R., Pichot, G., Poirriez, B., Erhel, J, 2013. Synthetic benchmark for modeling flow in 3D fractured media. Computers & Geosc. 50, 59-71.

Delay, F., Kaczmaryk, A., Ackerer, P., 2007. Inversion of hydraulic pumping tests in both homogeneous and fractal dual media. Adv. Water Resour. 30 (3), 314-334.

Delorme, M., Atfeh, B., Allken, V., Bourbiaux, B., 2008. Upscaling improvement for heterogeneous fractured reservoir using a geostatistical connectivity index, Geostats 2008, Santiago, Chile.

Dershowitz, W., Wallman, P., Kinrod, S., 1991. Discrete fracture modelling for the Stripa site characterization and validation drift inflow predictions. Stripa Project Tech. Rep. 91–16. SKB Swedish Nuclear Fuel and Waste Management Co., Sweden, Stockholm

Dverstorp, D., Anderson, J., Nordqvist, W., 1992. Discrete fracture network interpretation of field tracer migration in sparsely fractured rock. Water Resour. Res. 28 (9), 2327-2343.

Fourno, A., Grenier, C., Delay, F., Benabderrahmane, H., 2007. Development and qualification of a smeared fracture modelling approach for transfers in fractured media. Groundwater in fractured rocks, IAH selected paper series, 9 (6), 646 pp.

Geier, J.E., Doe, T.W., Benabderrahmane, A., and Hässler, L., 1996. Generalized radial-flow interpretations of well tests for the SITE-94 Project: SKI Report 96:4, Swedish Nuclear Power Inspectorate, Stockholm.

GEOTRAP, 2002. Radionuclide retention in geologic media. Workshop proceedings. Oskarshamn, Sweden, May 2001.

Gomez-Hernandez, J.J., Hendricks Franssen, H.J.W.M., Sahuquillo, A., 2000. Calibration of 3-D transient groundwater flow models for fractured rock. Calibration and reliability in groundwater modelling. IAHS publ. 265, 185-194.

Grenier, C., Benet, L.V., 2002. Groundwater flow and solute transport modelling with support of chemistry data, Task 5, Äspö Task force on groundwater flow and transport of solutes, SKB International Cooperation Report, IPR-02-39.

Grenier, C., Bernard-Michel, G., Benabderrahmane, H., 2009. Evaluation of retention properties of a semi-synthetic fractured block from modelling at performance assessment time scales (Äspö Hard Rock Laboratory, Sweden). Hydrogeol. J., 17 (5), 1051-1066.

Hirano, N., Ishibashi, T., Watanabe, N., Okamoto, A., Tsuchiya, N., 2010. New concept discrete fracture network model simulator, GeoFlow and three dimensional channeling flow in fracture network. Proceedings World Geothermal Congress.

Iding, M., Ringrose, P.S., 2009. Evaluating the impact of fractures on the long-term performance of the In Salah CO2 storage site. Energy Procedia 1 (1), 2021-2028.

Karimi-Fard, M., Durlofsky, L.J., Aziz, K., 2004. An efficient discrete-fracture model applicable for general-purpose reservoir simulators. Soc. Petrol. Eng. J. 9(2), 227-236.

Karimi-Fard, M., Gong, B., Durlofsky, L.J., 2006. Generation of coarse-grid continuum flow models from detailed fracture characterizations. Water Resour. Res. 42, W10423.

Koudina, N., Gonzales-Garcia, R., Thovert, J-F., Adler, P-M., 1998. Permeability of three-dimensional fracture networks. Phys. Rev. E 57 (4), 4466-4479.

Langevin., C., 2003. Stochastic ground water flow simulation with a fracture zone continuum model. Ground Water 41 (5), 587-601.

Lee, C.H., Deng, B.W., Chang, J.L., 1995. A continuum approach for estimating permeability in naturally fractured rocks. Eng. Geol. 39 (1-2) 71-85.

Long, J.C.S., Remer, J.S., Wilson, C.R., Witherspoon, P.A., 1982. Porous media equivalent for networks of discontinuous fractures. Water Resour. Res. 18 (3), 645-658.

Moreno, L., Neretnieks, I., 1993. Fluid flow and solute transport in a network of channels. J. Contam. Hydrol. 14 (3-4), 163-192.

Mosé, R., Siegel, P., Ackerer, P., Chavent, G., 1994. Application of the mixed hybrid finite element approximation in a groundwater flow model: luxury or necessity? Water Resour. Res. 30 (11), 3001-3012.

Neuman, S.P., 2005. Trends, prospects and challenges in quantifying flow and transport through fractured rocks. Hydrogeol. J. 13 (1), 124-147.

Nœtinger, B., Jarrige, N., 2012.. A quasi steady state method for solving transient Darcy flow in complex 3D fractured networks. J. Comput. Phys. 231 (1), 23-38.

Oda, M., 1985. Permeability tensor for discontinuous rock masses. Geotechnique 35, 483-495.

Oda, M., 1986. An equivalent continuum model for coupled stress and fluid flow analysis in jointed rock masses. Water Resour. Res. 22 13, 1845-1856.

Pan, J.B., Lee, C.C., Lee, C.H., Yeh, H.F., Lin, H.I., 2010. Application of fracture network model with crack permeability tensor on flow and transport in fractured rock. Eng. Geol. 116 (1-2), 166-177.

Pichot, G., Erhel, J., de Dreuzy, J-R., 2010. A mixed hybrid Mortar method for solving flow in discrete fracture networks. Applicable Analysis: An International Journal 89 (10), 1629-1643.

Reeves, D.M., Benson, D.A., Meerchaert, M.M., 2008. Transport of conservative solutes in simulated fracture networks: 1. Synthetic data generation. Water Resour. Res. 44, W05404.

Ringrose, P.S., Roberts, D.M., Gibson-Poole, C.M., Bond, C.,Wightman, M., Taylor, M., Raikes, S., Iding, M., Ostmo, S., 2011. Characterisation of the Krechba CO2 storage site: Critical elements controlling injection performance. Energy Procedia 4, 4672-4679.

Selroos, J.O.,Walker, D.D., Ström, A., Gylling, B., Follin, S., 2002. Comparison of alternative modelling approaches for groundwater flow in fractured rock. J. Hydrol. 257 (1-4), 174-188.

Svensson, U., 2001a. A continuum representation of fracture networks. Part I: Method and basic test cases. J. Hydrol. 250 (1-4), 170-186.

Svensson, U., 2001b. A continuum representation of fracture networks. Part II: Application to the Aspo hard rock laboratory. J. Hydrol. 250 (1-4), 187-205.

Tanaka, Y., Minyakawa, K., Igarashi, T., Shigeno, Y., 1996. Application of 3-D smeared fracture model to the hydraulic impact of the Äspö tunnel. SKB Report. ICR 96-07.

Tsang, C.F., Neretnieks, I., 1998. Flow channeling in heterogeneous fractured rocks. Rev. Geophys. 36 (2), 275–298.

Tsang, Y.M., Tsang, C.F., Hale, F.V., 1996. Tracer transport in a stochastic continuum model of fractured media. Water Resour. Res. 32 (10), 3077-3092.

Ubertosi, F., Delay, F., Bodin, J., Porel, G., 2007. A new method for generating a pipe network to handle channelled flow in fractured rocks. C.R. Geosciences 339 (10), 682-691.

Warren, J.E., Root, P.J., 1963. The behavior of naturally fractured reservoirs, SPE J. 3 (3), 245-255.

Younes, A., Ackerer, P., Delay, F. 2010, Mixed finite element for solving diffusion-type equations. Rev. Geophys. 48, RG 1004.